



HAL
open science

Frequency-resolved characterization of broadband two-color air-plasma terahertz beam profiles

Mattias Rasmussen, Oliver Nagy, Stefan Skupin, Alexandre Stathopoulos, Luc Bergé, Peter Uhd Jepsen, Binbin Zhou

► **To cite this version:**

Mattias Rasmussen, Oliver Nagy, Stefan Skupin, Alexandre Stathopoulos, Luc Bergé, et al.. Frequency-resolved characterization of broadband two-color air-plasma terahertz beam profiles. *Optics Express*, 2023, 31 (6), pp.9287. 10.1364/OE.482995 . hal-04009606

HAL Id: hal-04009606

<https://hal.science/hal-04009606>

Submitted on 1 Mar 2023

HAL is a multi-disciplinary open access archive for the deposit and dissemination of scientific research documents, whether they are published or not. The documents may come from teaching and research institutions in France or abroad, or from public or private research centers.

L'archive ouverte pluridisciplinaire **HAL**, est destinée au dépôt et à la diffusion de documents scientifiques de niveau recherche, publiés ou non, émanant des établissements d'enseignement et de recherche français ou étrangers, des laboratoires publics ou privés.



Frequency-resolved characterization of broadband two-color air-plasma terahertz beam profiles

MATTIAS RASMUSSEN,¹  OLIVER NAGY,¹  STEFAN SKUPIN,² 
ALEXANDRE STATHOPOULOS,^{3,4}  LUC BERGÉ,^{3,4}  PETER UHD
JEPSEN,¹  AND BINBIN ZHOU^{1,*} 

¹Department of Electrical and Photonics Engineering, Technical University of Denmark, Ørsted's Plads Bld. 343, 2800 Kgs. Lyngby, Denmark

²Institut Lumière Matière, UMR 5306 Université Lyon 1 – CNRS, Université de Lyon, Villeurbanne, France

³CEA, DAM, DIF, 91297 Arpajon, France

⁴CEA, LMCE, 91680 Bruyères-le-Châtel, France

*zhou@dtu.dk

Abstract: The frequency-resolved terahertz (THz) beam profile characteristics of a two-color air-plasma THz source were investigated in the broadband frequency range (1-15 THz). The frequency resolution is achieved by combining THz waveform measurements and the knife-edge technique. Our results show that the THz focal spot size is strongly frequency dependent. This has important implications on nonlinear THz spectroscopy applications where accurate knowledge of the applied THz electrical field strength onto the sample is important. In addition, the transition between the solid and hollow beam profile of the air-plasma THz beam was carefully identified. Far from the focus, the features across the 1-15 THz range have also been carefully examined, revealing the characteristic conical emission patterns at all frequencies.

© 2023 Optica Publishing Group under the terms of the [Optica Open Access Publishing Agreement](#)

1. Introduction

After more than two decades since Cook and Hochstrasser [1] first reported efficient two-color terahertz (THz) generation in air, the field of THz air photonics has firmly cemented its role as the toolbox of choice for generating and detecting ultra-broadband high-energy THz transients. These transients have found their applications within ultra-broadband and nonlinear THz time-domain spectroscopy (THz-TDS), and have allowed material scientists to probe nonlinear THz-matter interactions on different materials in the previously hard-to-reach frequency range [2]. The generation methods use femtosecond (fs) laser amplifiers providing ultrashort near-infrared pulses, which induce an elongated plasma filament when focused onto a gas [3–6]. The fs laser pulse together with its second harmonic, produced by a frequency-doubling nonlinear crystal, provide an asymmetric electric field in the generated plasma, resulting in a net transverse photocurrent and the subsequent radiation of THz transients. The near dispersion-free and self-replenishing nature of air simultaneously allows for ultra-broad bandwidth (>20 THz) and strong electric field strengths (>MV/cm). The corresponding air-biased coherent detection (ABCD) scheme exploits the third-order nonlinearity of air in order to directly sample the THz electric field and provides a detection bandwidth only limited by the duration of the near-infrared probe pulse [7,8]. As the bandwidth and peak electric field strength attainable by contemporary air-plasma THz sources continually improve, the spatial distribution of frequencies within the THz beam is becoming an increasingly important quantity to understand.

Throughout the past decade, the conical emission pattern of the two-color air-plasma THz generation process has been under intensive investigation, in order to illuminate the underlying physical mechanisms behind the characteristic donut-shape. In 2012, You, Oh, and Kim [9]

presented a model that explains the observed conical emission pattern as a consequence of the off-axis phase-matching due to local THz emission along the plasma filament. Modifications and improvements to the model have since then been proposed, such as the inclusion of the interaction between the THz waves and the plasma filament itself [10], as well as the consideration of the Kerr-contribution from air [11–13]. Additionally, several experimental and numerical studies have provided complementary insights on the matter of the two-color air-plasma THz beam profile. While most reported experiments utilized raster scanned pyroelectric/Golay detectors or THz cameras [9,10,14–19], some also include THz bandpass filters for enhanced frequency resolution at certain specific frequencies [9,16–18], interferometric detection [11,15], angular THz-TDS [17,19], and knife-edge assisted THz-TDS up to 2 THz [20]. Despite these efforts, an accurate spatio-spectral distribution of the air-plasma THz beam profile and its evolution from focus to far-field still remain to be fully understood. For instance, far away from the focus, general consensus is that spectral content above 3-5 THz is always conical in nature, exhibiting a frequency-dependent angular distribution, whereas the lower frequency content has been subject to some debate. In the vicinity of the THz focus, the beam profile has been shown to collapse into a solid beam [14], but the details of the transition between solid and hollow beam profiles are yet to be further explored.

The knife-edge beam profiling technique combined with time-domain waveform measurements has been employed to characterize features of photoconductive antenna based THz emitters [21–23]. As mentioned above, it has also been used to study the strong spatial confinement of THz waves inside the two-color fs laser induced filament, albeit with the measured frequency only up to 2 THz [20]. As the knife-edge assisted THz-TDS technique inherently provides accurate frequency resolution, careful implementation with a two-color air-plasma THz source combined with an ultra-broadband ABCD detection scheme could potentially lead to a more comprehensive and unified understanding of the complicated spatio-spectral properties of this uniquely important THz source.

Even though two-color air-plasma THz beam profiles have been intensively studied, and there is a common perception that the beam profile could vary significantly between very high and low frequencies; detailed frequency-resolved characterization of such broadband-by-nature THz emission across its ultra-broad bandwidth is very desire but still missing, primarily due to the poor availability of high-performance bandpass filters and flat-response imagers in the broad THz spectral range. To fully exploit the ultra-broadband and high-energy air-plasma THz transients for spectroscopic applications, accurate information on the frequency-dependent THz field distribution is important. In this work, we apply knife-edge assisted THz-TDS, to characterize frequency-resolved two-color air-plasma THz beam profiles in the extended frequency range of 1-15 THz. We measure the frequency dependent THz beam profile both near and far away from the focal plane. Our results show a strongly frequency-dependent focal spot size, highlighting the advantage of our technique over using a microbolometer-based THz camera. This has important implications on the calibration of the actual peak electrical field strength in the THz focus. The intermediate zone, where the solid focus spot transitions into a hollow beam profile, was carefully identified. We also examined the hollow, donut-shaped beam profile in the region far from the THz focus (= "far-field") and the frequency-dependence of its divergence angle. The experimental measurements agree well with the aforementioned model [9], relying on the dephasing between the two colors of the pump pulse along the plasma channel. Our findings contribute to further understanding of the fundamental two-color air-plasma THz generation physics, and provide important information for linear and nonlinear THz-TDS based on two-color air-plasma THz sources, where accurate knowledge of the frequency-resolved THz beam profile, near or far away from the THz focal plane, is important.

2. Experimental details

Figure 1(a) shows our experimental setup driven by a commercial Ti:sapphire laser amplifier with a 1 kHz repetition rate and a pulse duration of ≈ 40 fs. The 800 nm output (5.5 mm FWHM beam diameter, 0.9 mJ pulse energy before second harmonic generation), together with its 400 nm second harmonic, generated from an inline β -barium borate (BBO) crystal ($\theta = 29.2^\circ$, $\phi = 90^\circ$, 100 μm thick, approximately 35% second harmonic conversion efficiency), are employed to drive the plasma. An ultra-thin (45 μm) dual wavelength waveplate is inserted after the BBO to ensure horizontal polarization of both the 800 nm beam and its second harmonic. Due to the 300 mm lens (L1) in front of the BBO crystal, the two-color beam is focused into a nitrogen-purged atmosphere (focal spot size ≈ 40 μm) in order to generate ≈ 0.2 μJ ultra-broadband THz transients. Four off-axis parabolic mirrors (OPM) collimate and focus the THz beam (the first OPM has a 4" effective focal length, and the others 3"), resulting in one intermediate focus and one final focus at the high voltage (HV) electrodes, where an ABCD system, in conjunction with a variable delay stage and an avalanche photodiode (APD), is used for THz waveform sampling. The residual pump laser is blocked by a high-resistivity silicon wafer, which has previously been reported to affect the THz beam profile due to photoinduced carriers when placed close to the plasma [19]. However, with the silicon inserted in the collimated beam path, we did not measure any noticeable impact of photocarriers on the THz beam profile. Specifically, the measured THz beam profiles did not show any difference when inserting an additional teflon filter before or after the silicon wafer (the teflon filter blocks 99.9 % of the residual laser beam when placed in front of the silicon wafer). This minimal impact of photocarriers could be attributed to different spatial distributions between the THz transients and the residual laser pulses and/or the fact that the THz waves might arrive before the photocarrier density fully builds up. The reliable bandwidth of the experimental setup is ≈ 0.5 -20 THz. The OPM focusing system was carefully aligned using a THz camera, in order to minimize irregularities caused by focusing misalignment. It is also worth mentioning that THz emission from optical rectification of the BBO crystal has a negligible influence. At any point along the THz beam path, a sharp metallic knife-edge on a motorized linear stage may sequentially be translated across the THz beam (in either the horizontal or vertical direction), from fully unblocked to fully blocked. For each knife-edge step, a full THz waveform is recorded, resulting in a dataset as illustrated in Fig. 1(b), with corresponding spectra as seen in Fig. 1(c), obtained by Fourier transformation. In Fig. 1(b) and (c), the knife-edge is translated by 0.3 mm between each waveform/spectrum shown. From these THz spectra, any desired frequency component may be selected, and the THz spectral power, P_{THz} , can be plotted as a function of knife-edge position (Fig. 1(d) shows an example using the 4 THz component), allowing us to study the spatial distribution of the selected THz frequency within the beam. The minimum bandwidth of the selected THz component is determined by the length of the temporal window used in the waveform detection. In this work, we use a single frequency from the calculated spectra, resulting in a bandwidth of ≈ 0.4 THz. In the case of a Gaussian transverse beam profile, the knife-edge profile takes the form of a complementary error function, $P_{\text{THz}} \propto \text{erfc} \left[\sqrt{2}(x - x_0)/w \right]$, where x is the knife-edge position, x_0 a fit parameter, and w is the $1/e^2$ width of THz beam. The black curve in Fig. 1(d) shows an example of such a fit, where the discrepancy between fit and data indicates a non-Gaussian beam profile. To explain the features of the knife-edge profiles that are not encompassed by the simple error function fits, knife-edge profiles constructed from numerically generated beam intensity profiles with hollow shapes are produced, as illustrated by the green curve in Fig. 1(d), which was constructed by simulating a horizontally (left-to-right) moving knife-edge across the numerical beam profile in

the inset. A simple radially symmetric donut-shaped transverse beam profile is generated by

$$I_{\text{donut}}(r) = \exp\left(-2\frac{(r - r_{\text{donut}})^2}{w_{\text{donut}}^2}\right) + \exp\left(-2\frac{(r + r_{\text{donut}})^2}{w_{\text{donut}}^2}\right), \quad (1)$$

where r_{donut} is the radius of the ring, and w_{donut} is the width of the donut-ring itself. The second term ensures that $\partial_r I_{\text{donut}}(r)|_{r=0} = 0$, and is relevant for beam profiles with a small radius compared to the donut-width ($r_{\text{donut}} \leq w_{\text{donut}}$). In the case where $r_{\text{donut}} = 0$, the two terms fully overlap, and the intensity distribution reduces to a Gaussian distribution. This radially symmetric donut profile is then modified in various ways to account for the possible non-symmetric features seen in the data, e.g., multiplication by a linear gradient map to account for the aforementioned asymmetry, or anisotropic scaling to account for astigmatism (see [Supplement 1](#) for more details). In Fig. 1(d), the typical signature in knife-edge measurements of a hollow beam profile is shown by the green curve: near the middle of the curve (corresponding to the center of the beam), the slope is smaller than that of the Gaussian fit, whereas it is steeper towards the outer ends.

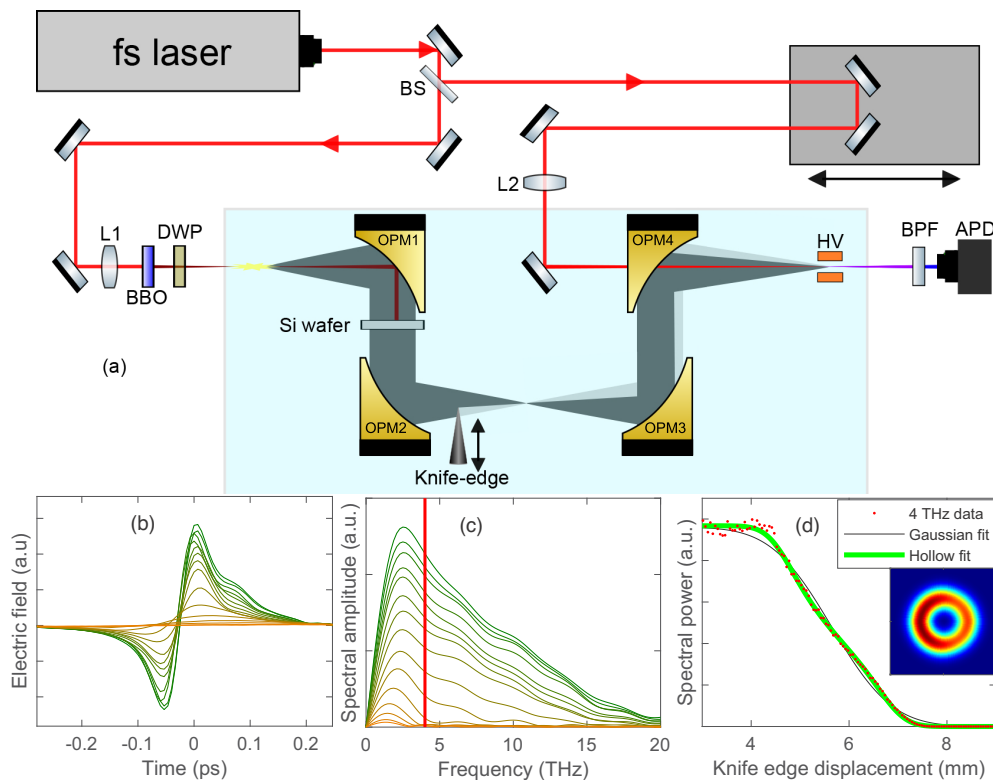


Fig. 1. (a) Schematic of the air-based experimental THz-TDS setup, with the inclusion of a metallic knife-edge to variably block the THz beam. (b) A typical dataset consisting of many THz waveforms, and (c), their corresponding spectra (linear scale), with the red line marking an arbitrary THz frequency (here 4 THz). With each successive waveform/spectrum shown, the knife-edge has moved by 0.3 mm. (d) The spectral power of the chosen 4 THz component as a function of the knife-edge position. The black curve shows an error function fit, corresponding to a Gaussian beam profile, whereas the green curve is the horizontal knife-edge profile of the numerically generated hollow beam profile shown in the inset.

One limitation of the knife-edge assisted THz-TDS is the inherent ambiguity of the measured knife-edge profiles, arising from the inability to resolve the beam intensity distribution perpendicular to the knife-edge movement, e.g., for a horizontally moving knife-edge alone, we cannot extract any information regarding the vertical distribution of the measured signal. This issue is compounded by the fact that the far-field THz beam profiles generated by the 40 fs laser are often slightly asymmetric, due to the spatial walk-off between the fundamental and second harmonic in the BBO crystal for in-line SH generation, and can therefore not simply be assumed to be circularly symmetric. This asymmetric behavior is both observed experimentally in the knife-edge data, in the THz camera images, as well as in our numerical simulations. The ambiguity of the knife-edge profiles can be largely alleviated by using two complementary measurements: one measured with vertical knife-edge movement, and one measured with horizontal knife-edge movement. Constructing a numerical beam profile which simultaneously reproduces both the vertical and horizontal knife-edge data much more reliably reveals the true transverse profile of the THz beam.

In brief, from the knife-edge assisted THz-TDS data we can construct knife-edge profiles (THz power as function of knife-edge position) for any frequency component, at any location along the THz propagation axis, and from these quantify the size and shape of the transverse THz beam profile. We note that, in general, the absolute noise at the left (unblocked THz beam) end of the knife-edge profiles is more severe than at the right (blocked THz beam) end, due to the increased influence of pump laser fluctuations.

3. Results

Prior to the knife-edge characterization, THz camera (uncooled microbolometer, NEC-T0831) beam profile measurements sweeping through the focal plane were taken, which indicate a few-mm zone with a solid focus spot, and a hollow donut beam profile away from the focal plane, which agrees fairly well with previous experimental work [14]. As a first step, we focus on the knife-edge assisted measurements around the few-mm focal zone exhibiting a solid THz beam profile, which is also the relevant sample insertion location for most of air-plasma THz-TDS applications.

3.1. Near the THz focus

For the solid THz beam focal spots, the measured frequency dependent knife-edge curves can be well fitted by Gaussian intensity profiles. Figure 2(a) shows the THz FWHM extracted from error function fits across the focal region between 2nd and 3rd OPM, for five frequency components. The inset shows a zoom-in near the spectroscopically important THz focus (black rectangle), showing a strongly frequency-dependent THz spot size. The shaded zone in Fig. 2(a) highlights the region where the knife-edge curves for all measured THz frequencies are well-fitted by error functions (not shown), indicating that the beam profile has collapsed into a solid near-Gaussian. Outside the shaded region, the frequency dependent knife-edge curves are not all well-fitted by error function curves anymore, which indicates that the transverse THz beam profiles significantly deviate from Gaussians. Therefore, this shaded region should provide the optimal sample location when performing spectroscopy. Special care should be taken if nonlinear THz spectroscopy data is to be collected on a sample placed outside of these boundaries, due to the non-trivial spatio-spectral distribution and its influence on light-matter interactions depending on the absolute field strength.

The experimentally extracted frequency-dependent spot size at the beam waist is shown in Fig. 2(b), together with the theoretical value for a diffraction-limited Gaussian beam focus, given by $\text{FWHM} = 2\sqrt{2 \ln 2} \lambda_{\text{THz}} \zeta(\lambda_{\text{THz}}) / \pi$, where $\zeta(\lambda_{\text{THz}})$ is the effective f-number of the focusing system in our setup [24], which takes the frequency-dependent THz beam size impinging on the focusing mirror into account. The impinging beam sizes were extracted as the difference in

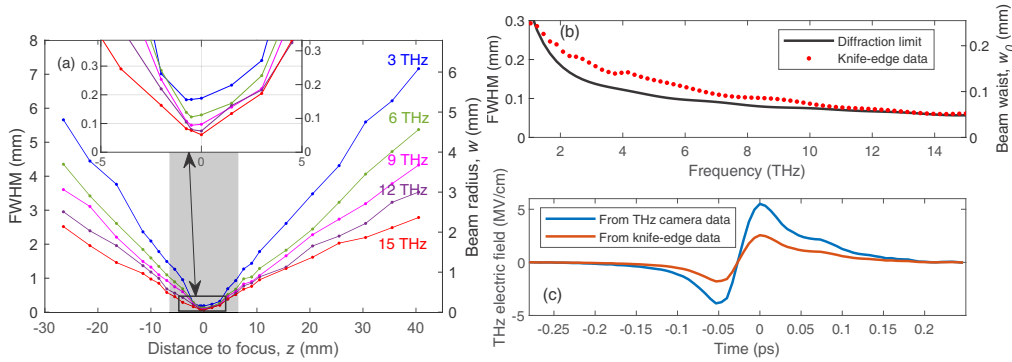


Fig. 2. (a) THz FWHM across the focal zone (between 2nd and 3rd OPM), for five different frequency components. The inset shows a zoom-in of the black rectangle near the immediate focus. The shaded area highlights the region where the beam exhibits a solid Gaussian intensity profile for all frequencies. (b) FWHM/beam radius as function of frequency. The red dots are values extracted from knife-edge data, and the black curve is the theoretical diffraction-limited value for a Gaussian beam focused by an OPM. (c) Example of THz electric field calibration (encompassing the whole spectrum of Fig. 1(c)) performed with a single THz spot size extracted by THz camera (blue) versus a frequency-weighted spot size from the knife-edge data (red).

knife-edge position between 95% and 5% THz transmission, from knife-edge profiles with the knife-edge in the collimated region (between 1st and 2nd OPM), and, due to the asymmetry of the far-field profiles, have some degree of uncertainty, which carries over to the plotted diffraction limit. The relatively low signal-to-noise ratio at the upper and lower extremes of the 1-15 THz spectrum also presents an additional source of uncertainty. Although our THz beam evidently has a donut-shaped far-field profile, and is therefore not a Gaussian beam, we see that the THz focal spot size is close to the diffraction limit at the lower and higher ends of the detected spectrum, whereas the intermediate part deviates more significantly. The deviations in the mid-frequency range are subject to further studies, but we note that the theoretical diffraction limit applied here is valid for a Gaussian beam, and we observe clear non-Gaussian behavior of the beam.

In Fig. 2(c), we illustrate the impact of using an accurately extracted frequency-dependent THz spot size, where the electric field strength of a THz waveform has been calibrated for two different THz spot size values, using the following equation [25]:

$$E(t) = \frac{\mathcal{E}_m(t)}{\max_t(|\mathcal{E}_m(t)|)} \sqrt{\frac{2\eta_0 U}{\int dx dy \mathcal{G}(x, y) \int dt \frac{|\mathcal{E}_m(t)|^2}{\max_t(|\mathcal{E}_m(t)|^2)}}, \quad (2)$$

where $\mathcal{E}_m(t)/\max_t(|\mathcal{E}_m(t)|)$ is the normalized THz waveform, $\eta_0 = 377 \Omega$ is the vacuum impedance, U is the THz pulse energy, and $\mathcal{G}(x, y)$ is the Gaussian spatial intensity profile of the THz beam, which depends on the spot size. This equation is a somewhat crude approximation, since the transverse spatial beam profile obviously has a spectral dependence and therefore cannot be separated from its temporal profile, but is nonetheless a widely used tool for estimating the electric field strength of a given THz source. In the first case (blue waveform), the THz spot size was extracted by fitting a Gaussian to an image from a THz camera. The THz camera has an uncalibrated frequency sensitivity, but is suspected to overemphasize the more energetic high-frequency THz photons, leading to an underestimated spot size, due the increased focusability of higher frequencies. This, in turn, leads to an overestimation of the THz electric field strength. In the second method (red waveform), the THz spot size is calculated using the

knife-edge extracted spot sizes as a frequency-dependent power-weighted average:

$$w_{0,\text{weighted}} = \frac{\int P_{\text{THz}}(\omega)w_0(\omega) d\omega}{\int P_{\text{THz}}(\omega) d\omega}, \quad (3)$$

where $w_0(\omega)$ is now the frequency-dependent spot size extracted from the knife-edge data. In the example shown, the difference between the two methods is approximately a factor 2, which is a sizeable discrepancy when working with, e.g., field-sensitive nonlinear spectroscopy.

3.2. Intermediate region

We now turn our attention to the transition between the solid beam profile at the THz focus and the hollow beam profile in the far-field, i.e., the region near the edge of the shaded area in Fig. 2(a). In Fig. 3, knife-edge profiles (dots) and their numerical derivatives (dashed lines) are shown for 3, 6, and 9 THz, and for each of the three regions: (a) near the THz focus, where the beam profile is mostly Gaussian, (c) far away from the focus, where the beam profile exhibits hollow features, and (b) in the transitional zone between (a) and (c). In (a), the differentiated knife-edge profiles exhibit mostly single-peak and near-Gaussian profiles for all the three frequency components. The frequency-dependence of the spot size is clearly visible, with the 9 THz component being narrower than those at the lower frequencies. In (b), we see that the splitting starts to appear, with a double peak emerging in all three frequency components. This feature corresponds to the suppression of on-axis radiation in the THz beam profile, i.e., a hollowing of the beam profile. In (c), all three frequency components now clearly exhibit double-peaked structures, indicating that the beam profile has fully opened up into a donut-shape. In this case still, we observe that the overall transverse size of the knife-edge curve is smaller for higher frequencies, meaning that the conical emission angle decreases for increasing frequency, in agreement with previous studies [9,11,16].

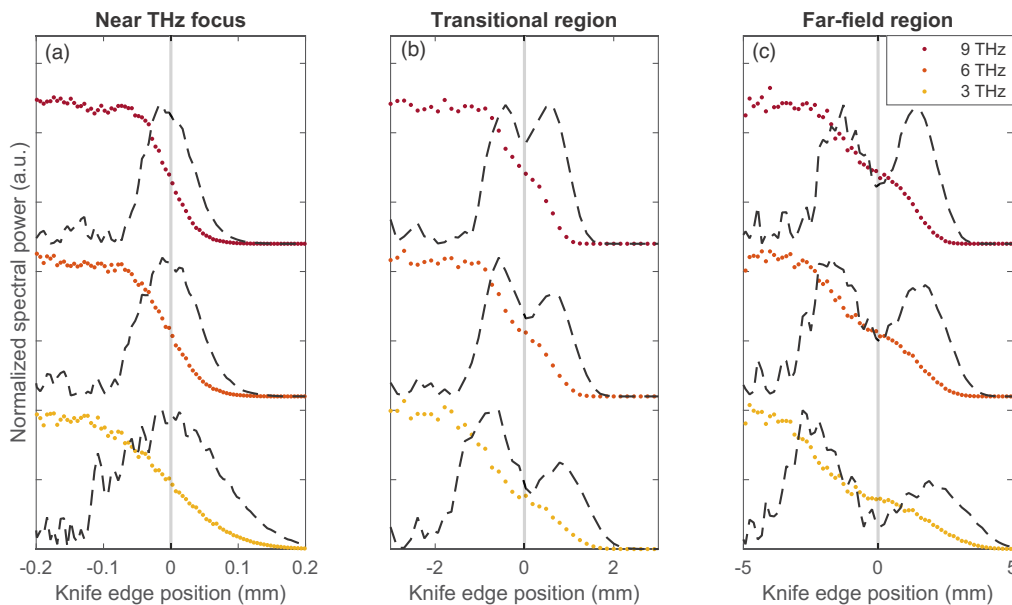


Fig. 3. Experimental knife-edge profiles for 3, 6, and 9 THz at three locations (offset for clarity): (a) Near the THz focus, (b) at the transitional region, and (c) far from the THz focus. The dashed lines are the numerical derivatives of the knife-edge profiles.

3.3. Far from the THz focus

Moving farther away from the focus, we now examine the far-field region, where the THz beam profile has opened up considerably, exhibiting its characteristic hollow shape. This hollowing of the THz beam profile introduces significant deviations between the experimental knife-edge profiles and the attempted error function fits, and these deviations must be accounted for by using non-Gaussian beam profiles. As previously mentioned we employ two complementary knife-edge datasets to capture the asymmetry in the resulting beam profiles. Two such datasets are shown in Fig. 4(a) and (b), where the former dataset was collected with a horizontally moving knife-edge, and the latter with vertical movement. Specifically, we display knife-edge profiles from the collimated region (between OPM 1 and 2), for 1, 3, 6, and 9 THz, along with error function fits corresponding to Gaussian beam profiles (black curves). In order to encompass the deviating features of all four frequency components, we numerically generate the hollow THz beam profiles seen in Fig. 4(c)-(f) (see [Supplement 1](#) for details) and perform knife-edge simulations on them, resulting in the green curves seen in Figs. 4(a), (b). For example, the green curves for the 9 THz components in Fig. 4(a) and 4(b) are both generated by simulating a knife-edge translation across the same numerical beam profile, Fig. 4(c). In this way, differences between vertical and horizontal knife-edge profiles can be explained by asymmetry (e.g., BBO walk-off as previously discussed), astigmatism (more evident in the lower frequencies), and other beam imperfections.

We see that the the knife-edge profiles generated by the hollow beam profiles accurately represent the experimental knife-edge data. In Fig. 4(g), the four generated beam profiles from Fig. 4(c)-(f) are weighted by their respective spectral power (Fig. 1(c)) and added together. The resulting beam profile in Fig. 4(g) is thus an approximation of the true THz beam intensity profile: in this case using four frequency components, but in practice extendable to any frequency resolution supported by the THz-TDS data. This can be compared to the beam profile obtained from a THz camera, as seen in Fig. 4(h). The camera sensor was too small to capture the full THz beam profile in the collimated beam, so the image was obtained after the focus, in the far-field between OPM 2 and 3. Its size is therefore not comparable to Fig. 4(g), but the general shape of the beam profile shows good qualitative agreement to one generated from knife-edge data. Figure 4(i) shows a far-field beam profile obtained from unidirectional 3D simulations (see [Supplement 1](#) for more details), where the inclusion of the aforementioned spatial walk-off gives rise to the qualitatively similar asymmetric beam profile seen in Figs. 4(g), (h).

In Fig. 5(b), we show the frequency-angular spectrum experimentally obtained in the far-field, based on the previously discussed fits to the frequency-resolved knife-edge profiles. The 0° angle corresponds to the center of the constructed beam profiles, i.e., $r = 0$ in Eq. (1). The original power spectrum measured by THz-TDS is recovered after integration over the emission angle for each frequency component, see Fig. 5(a). In general, we see that none of the frequencies have their maximum on the optical axis, indicating that the THz emission is conical throughout the 1-15 THz range, with the divergence angle decreasing from 9° to 2° and reaching a maximum at about 3° - 5° . Additionally, the cone angle decreases with increasing frequency. The results agree very well with multiple previous studies [9,10,16]. It has been previously been reported that the radiation pattern from an elongated electromagnetic source follows the relation $\delta \propto 1/\sqrt{\nu_{\text{THz}}}$ [18], which is largely in agreement with our data and illustrated by the dashed line in Fig. 5(b).

In Fig. 5(c) we present the semi-analytical frequency-angular spectrum obtained from You et al.'s model [9] that predicts off-axis emission of the generated THz field. This model is based on the phase-mismatch between the two colors, depending on their respective optical and plasma dispersion. In particular, the velocity mismatch between the harmonics induces a variation along the propagation axis into the polarization of the THz bursts, which are emitted by the photocurrents, given the laser intensity range employed in our setup. In particular, the amplitude of the photocurrents vary with $\sin \theta$, θ being the varying phase shift between the two optical

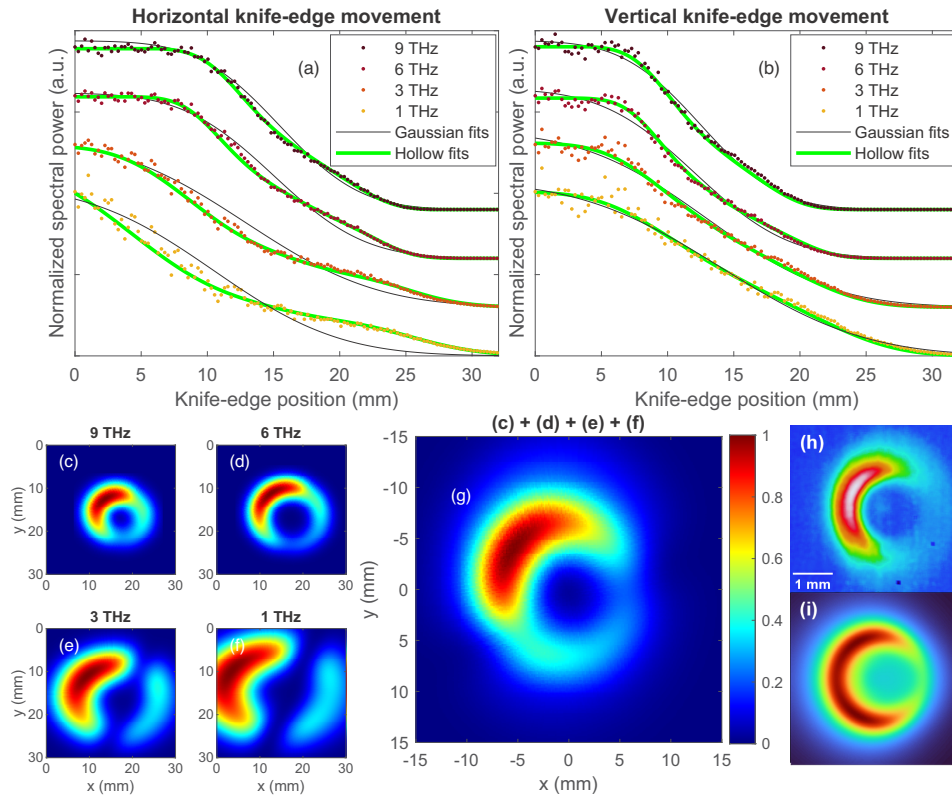


Fig. 4. Far-field beam profiles. (a) Knife-edge profiles (horizontal knife-edge movement) for 1, 3, 6, and 9 THz, along with fits corresponding to Gaussian (black) and hollow (green) beam profiles (offset for clarity). (b) Same as (a), but with vertical knife-edge movement. (c)-(f) Numerically generated 1, 3, 6, and 9 THz beam profiles used for the hollow fits in (a) and (b). (g) The sum of the four beam profiles in (c)-(f), weighted with their respective spectral power. (h) THz camera image from the far-field region between OPM 2 and 3. (i) Far-field beam profile from unidirectional 3D simulations.

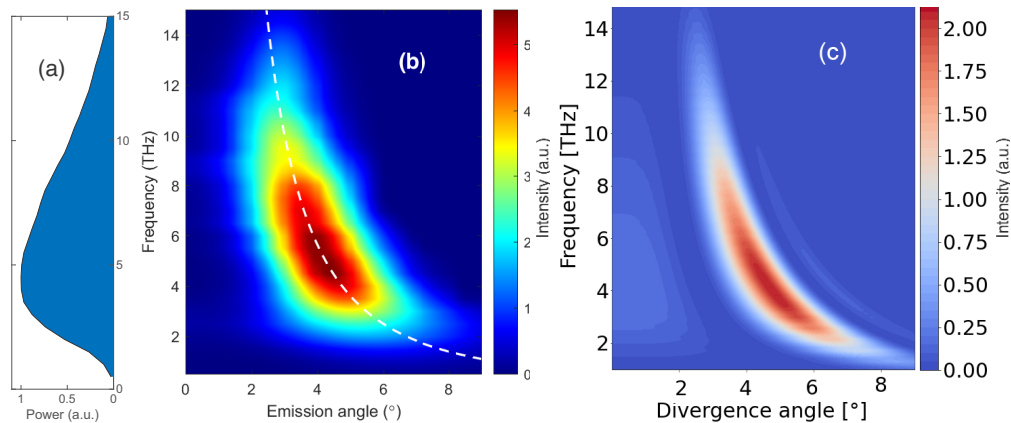


Fig. 5. (a) THz power spectrum recovered by integration of (b). (b) THz frequency-angular spectrum extracted from vertical knife-edge data in the far-field. The dashed line shows that the angle of peak intensity roughly follows a $\propto 1/\sqrt{\nu_{\text{THz}}}$ evolution. (c) Corresponding semi-analytical angular spectrum obtained with You et al.'s model [9].

components. The phase variations induced by a two-color pump along the plasma channel lead to interference between the generated THz pulses, resulting in a conical shaped emission in the far-field. By assuming that the emitting volume is a cylinder of radius a , length L , and with a homogeneous electron density, N_e , the dependency of the THz spectral power on frequency and emission angle is given by

$$P_r(\omega, \Theta) \propto L^2 a^4 |A(\omega)|^2 \left(\kappa_+^2 + \kappa_-^2 - 2\kappa_+ \kappa_- \cos(2\theta_0) \right) \left(\frac{J_1(\beta)}{\beta} \right)^2, \quad (4)$$

where $A(\omega)$ is the THz spectrum emitted by the plasma, $\kappa_{\pm} = \text{sinc} \left[\frac{1}{2} kL \left(1 - \cos \Theta \pm \frac{\lambda}{2l_d(N_e)} \right) \right]$, θ_0 an incident phase shift, $\beta = ka \sin \Theta$, $\lambda = 2\pi/k$ is the THz wavelength, and l_d is the N_e -dependent dephasing length, over which the two optical colors shift from 0 to π . It is given by $l_d = \lambda_{\text{FH}} / [4n(2\omega_0) - 4n(\omega_0)]$, where $n(\omega)$ is the refractive index that includes both linear and plasma response and λ_{FH} is the fundamental laser wavelength. Equation (4) implies that the privileged emission angle of the THz waves generated by a plasma is described by $\cos \Theta = 1 - \lambda / [2l_d(N_e)]$, provided that the plasma length satisfies $L > l_d$. This condition is verified in the experimental setup of Fig. 1(a), as the generated plasma is about 2.5 cm long and the dephasing length is close to 1 cm for the density level evaluated at $N_e = 5 \times 10^{16} \text{ cm}^{-3}$. The latter value is consistent with measured density levels reported in [26] for a ratio between the input pulse width and focal length close to 0.01, and for a ratio of incident power over the critical power for self-focusing of 3. The plasma radius, $a = 50 \text{ }\mu\text{m}$, is extracted from the unidirectional 3D simulations discussed in Supplement 1. The squared absolute value of the THz spectrum $|A(\omega)|^2$ is obtained from the experimental measurements, including the ABCD detection function response. The semi-analytical calculation based on Eq. (4) gives a good agreement with the measured conical THz spectrum.

It is worth noting that the conical emission pattern in the low THz range (1-3 THz) was carefully verified by additional THz camera measurements assisted with appropriate THz filters in the lower spectral region. A typical conical feature can always be obtained when the THz camera sensor is gradually moved away from the focal zone. It was also noticed that non-optimal alignment from the BBO crystal or dual-wavelength wave plate inside the THz generation beam path would significantly distort the conical patterns. The distortion could bring certain ambiguity to the THz beam pattern, especially at the lower THz frequency range where the beam profile and the donut-ring width are much larger. In contrast, frequencies above 3 THz tend to maintain the donut shape, even with severe distortions, due to the sharp donut-ring feature.

4. Conclusion

To conclude, by combining the knife-edge technique and THz-TDS, we have investigated the frequency-resolved beam profile of a two-color air-plasma THz source in the ultra-broadband frequency range (1-15 THz). Our results show that the THz focal spot size is strongly frequency dependent, e.g., the focus spot of the 3 THz component is more than 3 times the size of 15 THz component. This strong frequency dependence has significant implication on nonlinear THz spectroscopy applications, where accurate knowledge of the applied THz electrical field strength onto the sample is important. The transition between the solid THz beam profile in the focal zone and the hollow beam profile in the far-field was also carefully investigated, and, finally, the far-field features across 1-15 THz have been carefully examined. A hollow donut-shape was clearly observed for all THz frequencies, with the divergence angle of the conical emission decreasing with increasing frequency. We hope that our results will not only be informative, especially for nonlinear THz spectroscopy applications based on high-energy air-plasma THz sources, but can also contribute to the fundamental understanding of two-color air-plasma THz generation physics.

Funding. Velux Fonden (00023215); Danmarks Frie Forskningsfond (THz-GRIP: 2035-00365B, ULTRA-TED: 9040-00360B); Agence Nationale de la Recherche (ANR-19-ASMA-0007); Grand Équipement National De Calcul Intensif (A0120507594); Qatar National Research Fund (NPRP 12S-0205-190047).

Disclosures. The authors declare no conflicts of interest.

Data availability. Data underlying the results presented in this paper are not publicly available at this time but may be obtained from the authors upon reasonable request.

Supplemental document. See [Supplement 1](#) for supporting content.

References

1. D. J. Cook and R. M. Hochstrasser, "Intense terahertz pulses by four-wave rectification in air," *Opt. Lett.* **25**(16), 1210–1212 (2000).
2. H. A. Hafez, X. Chai, A. Ibrahim, S. Mondal, D. Férachou, X. Ropagnol, and T. Ozaki, "Intense terahertz radiation and their applications," *J. Opt.* **18**(9), 093004 (2016).
3. M. Kress, T. Löffler, S. Eden, M. Thomson, and H. G. Roskos, "Terahertz-pulse generation by photoionization of air with laser pulses composed of both fundamental and second-harmonic waves," *Opt. Lett.* **29**(10), 1120–1122 (2004).
4. T. Bartel, P. Gaal, K. Reimann, M. Woerner, and T. Elsaesser, "Generation of single-cycle THz transients with high electric-field amplitudes," *Opt. Lett.* **30**(20), 2805–2807 (2005).
5. X. Xie, J. Dai, and X.-C. Zhang, "Coherent control of THz wave generation in ambient air," *Phys. Rev. Lett.* **96**(7), 075005 (2006).
6. K. Y. Kim, J. H. Glowina, A. J. Taylor, G. Rodriguez, W. P. Leemans, C. G. R. Geddes, J. Faure, C. Tóth, J. V. Tilborg, C. B. Schroeder, E. Esarey, G. Fubiani, D. Auerbach, B. Marcelis, M. A. Carnahan, R. A. Kaindl, J. Byrd, and M. C. Martin, "Terahertz emission from ultrafast ionizing air in symmetry-broken laser fields," *Opt. Express* **15**(8), 4577–4584 (2007).
7. J. Dai, X. Xie, and X. C. Zhang, "Detection of broadband terahertz waves with a laser-induced plasma in gases," *Phys. Rev. Lett.* **97**(10), 103903 (2006).
8. N. Karpowicz, J. Dai, X. Lu, Y. Chen, M. Yamaguchi, H. Zhao, X. C. Zhang, L. Zhang, C. Zhang, M. Price-Gallagher, C. Fletcher, O. Mamer, A. Lesimple, and K. Johnson, "Coherent heterodyne time-domain spectrometry covering the entire "terahertz gap"," *Appl. Phys. Lett.* **92**, 011131 (2008).
9. Y. S. You, T. I. Oh, and K. Y. Kim, "Off-axis phase-matched terahertz emission from two-color laser-induced plasma filaments," *Phys. Rev. Lett.* **109**(18), 183902 (2012).
10. A. Gorodetsky, A. D. Koulouklidis, M. Massaouti, and S. Tzortzakis, "Physics of the conical broadband terahertz emission from two-color laser-induced plasma filaments," *Phys. Rev. A* **89**(3), 033838 (2014).
11. V. A. Andreeva, O. G. Kosareva, N. A. Panov, D. E. Shipilo, P. M. Solyankin, M. N. Esaulkov, P. G. D. A. Martínez, A. P. Shkurinov, V. A. Makarov, L. Bergé, and S. L. Chin, "Ultrabroad terahertz spectrum generation from an air-based filament plasma," *Phys. Rev. Lett.* **116**(6), 063902 (2016).
12. L. Bergé, S. Skupin, C. Köhler, I. Babushkin, and J. Herrmann, "3D numerical simulations of THz generation by two-color laser filaments," *Phys. Rev. Lett.* **110**(7), 073901 (2013).
13. A. Nguyen, P. G. de Alaiza Martínez, J. Déchard, I. Thiele, I. Babushkin, S. Skupin, and L. Bergé, "Spectral dynamics of THz pulses generated by two-color laser filaments in air: the role of Kerr nonlinearities and pump wavelength," *Opt. Express* **25**(5), 4720–4740 (2017).
14. P. Klarskov, A. C. Strikwerda, K. Iwaszczuk, and P. U. Jepsen, "Experimental three-dimensional beam profiling and modeling of a terahertz beam generated from a two-color air plasma," *New J. Phys.* **15**(7), 075012 (2013).
15. V. Blank, M. D. Thomson, and H. G. Roskos, "Spatio-spectral characteristics of ultra-broadband THz emission from two-colour photoexcited gas plasmas and their impact for nonlinear spectroscopy," *New J. Phys.* **15**(7), 075023 (2013).
16. Y. J. Yoo, D. Kuk, Z. Zhong, and K. Y. Kim, "Generation and characterization of strong terahertz fields from khz laser filamentation," *IEEE J. Sel. Top. Quantum Electron.* **23**(4), 1–7 (2017).
17. A. A. Ushakov, P. A. Chizhov, V. A. Andreeva, N. A. Panov, D. E. Shipilo, M. Matoba, N. Nemoto, N. Kanda, K. Konishi, V. Bukin, M. Kuwata-Gonokami, O. G. Kosareva, S. V. Garnov, and A. B. Savel'ev, "Ring and unimodal angular-frequency distribution of THz emission from two-color femtosecond plasma spark," *Opt. Express* **26**(14), 18202–18213 (2018).
18. D. E. Shipilo, N. A. Panov, I. A. Nikolaeva, A. A. Ushakov, P. A. Chizhov, K. A. Mamaeva, V. V. Bukin, S. V. Garnov, and O. G. Kosareva, "Low-frequency content of THz emission from two-color femtosecond filament," *Photonics* **9**(1), 17 (2022).
19. C. B. Sørensen, L. Guiramand, J. Degert, M. Tondusson, E. Skovsen, E. Freysz, and E. Abraham, "Conical versus gaussian terahertz emission from two-color laser-induced air plasma filaments," *Opt. Lett.* **45**(7), 2132–2135 (2020).
20. J. Zhao, W. Chu, Z. Wang, Y. Peng, C. Gong, L. Lin, Y. Zhu, W. Liu, Y. Cheng, S. Zhuang, and Z. Xu, "Strong spatial confinement of terahertz wave inside femtosecond laser filament," *ACS Photonics* **3**(12), 2338–2343 (2016).
21. H. Lin, C. Fumeaux, B. M. Fischer, and D. Abbott, "Modelling of sub-wavelength THz sources as gaussian apertures," *Opt. Express* **18**(17), 17672–17683 (2010).
22. M. Peccianti, M. Clerici, A. Pasquazi, L. Caspani, S. P. Ho, F. Buccheri, J. Ali, A. Busacca, T. Ozaki, and R. Morandotti, "Exact reconstruction of THz sub- λ source features in knife-edge measurements," *IEEE J. Select. Topics Quantum Electron.* **19**(1), 8401211 (2013).

23. M. Baillergeau, K. Maussang, T. Nirrengarten, J. Palomo, L. H. Li, E. H. Linfield, A. G. Davies, S. Dhillon, J. Tignon, and J. Mangeney, "Diffraction-limited ultrabroadband terahertz spectroscopy," *Sci. Rep.* **6**(1), 24811 (2016).
24. B. E. A. Saleh and M. C. Teich, *Fundamentals of Photonics*, 2nd edition (Wiley, 2007).
25. M. Clerici, M. Peccianti, B. E. Schmidt, L. Caspani, M. Shalaby, M. Giguè, A. Lotti, A. Couaïron, F. Légaré, T. Ozaki, D. Faccio, and R. Morandotti, "Wavelength scaling of terahertz generation by gas ionization," *Phys. Rev. Lett.* **110**(25), 253901 (2013).
26. F. Théberge, W. Liu, P. T. Simard, A. Becker, and S. L. Chin, "Plasma density inside a femtosecond laser filament in air: Strong dependence on external focusing," *Phys. Rev. E* **74**(3), 036406 (2006).